Supporting Material for "Worm-like Ising model for protein mechanical unfolding under the effect of osmolytes"

Daniel Aioanei[1], Marco Brucale[2], Isabella Tessari[3], Luigi Bubacco[3], Bruno Samorì[1]

[1] Department of Biochemistry 'G.Moruzzi', University of Bologna, Italy
and
S3 Center of Nanostructures and Biosystems at Surfaces, Istituto di Nanoscienze—CNR (Italy)

[2] CNR, Institute of Nanostructured Materials (ISMN), Via Salaria Km 29300, 00015 Monterotondo Stazione, Rome, Italy

[3] Department of Biology, University of Padova, Via Ugo Bassi 58b, 35121 Padova, Italy

S1 The model

S1.1 Solving the thermodynamics of the WSME model and its extension for the osmolyte effect

It can be seen that compared to Eq. 1 in the main text of the original WSME model, the effective free energy expression of Eq. 5 has one extra term for each native stretch. Because no terms are introduced that simultaneously involve peptide bonds from multiple native stretches, the transfer-matrix exact solution to the thermodynamics of the WSME model (1) is equally applicable when the osmolyte effect is incorporated. In this section we reiterate the equations to exactly compute, for two common order parameters, the free energy landscape of the WSME model extended with the osmolyte effect (2) (see Eq. 5), and of the original WSME model (see Eq. 1), which can be seen as the special case of zero osmolyte concentration.

Let us introduce the notation

$$Q_{ij} = 1K \times k_B\varepsilon \sum_{i<k<l<j} h_{kl} + k_B T \sum_{k=i+1}^{j-1} q_k + M_{ij}, \tag{S1}$$

for $0 \le i < j \le N+1$.

The two order parameters we consider are the number of native peptide bonds

$$\phi(\vec{m}) = \sum_{i=1}^{N} m_i \tag{S2}$$

and the weighted number of native contacts (3):

$$\theta(\vec{m}) = -\sum_{1 \le i < j \le N} h_{ij} \prod_{k=i}^{j} m_k. \tag{S3}$$

We denote generically by $\vec{g}$ a two-dimensional vector such that g_{ij} is either of the two mentioned order parameters of the native stretch delimited by peptide bonds i and j with $0 \le i < j \le N+1$, namely the number of peptide bonds $(j-i-1)$ or the weighted number of native contacts $(-\sum_{i<k<l<j} h_{kl})$.

Then the effective free energy E_p restricted to the states having the relevant order parameter (ϕ or θ) equal to p (more formally, $\sum_{0 \le k < l \le N+1} S_{kl} g_{kl} = p$) is computed as

$$E_p(\vec{g}) = R_{Np}(\vec{g}) - k_B T \sum_{k=1}^{N} q_k \quad \text{(S4)}$$

for $0 \le p \le g_{0,N+1}$ where the quantity $R_{Np}(\vec{g})$ is computed in polynomial time via the recursion

$$exp[-R_{ip}(\vec{g})/(k_B T)] = \delta_{p,g_{0,i+1}} exp[-Q_{0,i+1}/(k_B T)] + \sum_{(1\le j\le i)\wedge(g_{j,i+1}\le p\le g_{0,j}+g_{j,i+1})} exp[-R_{j-1,p-g_{j,i+1}}(\vec{g})/(k_B T) - Q_{j,i+1}/(k_B T)], \quad \text{(S5)}$$

with $\delta_{\cdot,\cdot}$ being the Kronecker delta symbol.

The average number of native peptide bonds in the absence of force, which is needed to fit the parameter ε, follows trivially once the free energy landscape is computed via Eq. (S4) for the number of native peptide bonds.

S1.2 Solving the thermodynamics under the effect of force

In this section we present the equations that allow one to compute in polynomial time the effective free energy as a function of the number of native peptide bonds ϕ, the weighted number of native contacts θ, and contour length L in the presence of a stretching force f. Herein we reuse the definitions of Q_{ij} (see Eq. (S1)) and $\vec{g}$ from Section S1.1.

The key to polynomial time computation of force-dependent effective free energies lies in the discretization of the possible lengths of native stretches l_{ij}. As in Ref. (4), we assume that a length scale is chosen such that the size of the set of all protein subchain contour lengths grows only linearly with increasing protein size.

It is useful to consider the maximum contour length D_i that the protein chain made up of the first i peptide bonds can take, $0 \le i \le N$. Note that fully denaturing the protein chain is not guaranteed to lead to the maximum contour length because of two reasons. One is due to rounding of the native stretch lengths, which in general is not guaranteed to preserve the triangle inequality. The other reason is that we assign to $l_{i,i+1}$ a value not dictated by the three-dimensional structure of the protein (see the main text), which again may, in principle, break the triangle inequality. The maximum contour length of the first i peptide bonds can be computed recursively as follows:

$$D_i = \max_{0 \le j \le i}[(1-\delta_{j,0})D_{j-1} + l_{j,i+1}]. \quad \text{(S6)}$$

The effective free energy as a function of contour length L and order parameter p (either the number of native peptide bonds ϕ or the weighted number of native contacts θ) in the presence of a stretching force f can be written as

$$E_{L,p}(\vec{g}, f) = U_{N,L,p} - k_B T \sum_{i=1}^{N} q_i - \xi F_{WLC}^{-1}(f)\, fL \quad \text{(S7)}$$

for $0 \le L \le D_N$ and $0 \le p \le g_{0,N+1}$, where $U_{N,L,p}$ is independent of force and it is computed recursively:

$$\begin{aligned} exp[-U_{iLp}(\vec{g})/(k_B T)] &= \delta_{L,l_{0,i+1}} \delta_{p,g_{0,i+1}} exp[-Q_{0,i+1}/(k_B T)] \\ &+ \sum_{(1 \le j \le i) \wedge (l_{j,i+1} \le L \le D_{j-1} + l_{j,i+1}) \wedge (g_{j,i+1} \le p \le g_{0,j} + g_{j,i+1})} \\ & exp[-U_{j-1,L-l_{j,i+1},p-g_{j,i+1}}(\vec{g})/(k_B T) - Q_{j,i+1}/(k_B T)] \end{aligned} . \quad \text{(S8)}$$

The average number of native peptide bonds in the presence of force, which is needed to fit the parameter ξ, follows trivially once the free energy landscape is computed via Eq. (S7) for the number of native peptide bonds.

It should be noted that while Eq. (S7) can be summed at zero force over the possible L values to yield the same thermodynamic quantities like Eq. (S4), the latter equation, specialized for the absence of force, is simply faster to evaluate in practice, when applicable.

S1.3 Continuous-time Markov chain approach to kinetics

A necessary condition for Monte Carlo simulations is that the associated kinetics satisfy the *balance* condition, i.e., that they leave the Boltzmann distribution invariant (5). Monte Carlo simulations are commonly designed to satisfy an even stronger condition called *detailed balance* (6) that implies reversibility of all transitions. We adopt the latter approach and define a continuous-time Markov chain by allowing single-bond flip transitions (7). More formally, we allow transitions $\overrightarrow{m^t} \to \overrightarrow{m^h}$ from a tail state $\overrightarrow{m^t}$ to a head state $\overrightarrow{m^h}$ whenever the two states differ by the native status of exactly one peptide bond. By assigning transition rates according to a detail-balance preserving prescription that depends only on the difference of the energetic levels of the tail and head states expressed in $k_B T$ units, e.g. the exponential, Metropolis or Glauber transition rate expressions (8), the continuous-

time Markov chain thus defined is in detailed balance with the Boltzmann distribution of states. Hereafter we denote the transition rate from tail state $\overrightarrow{m^t}$ to head state $\overrightarrow{m^h}$ by the notation

$$\begin{aligned} W(\overrightarrow{m^t},\overrightarrow{m^h}) &= W\left([H_O(\overrightarrow{m^h}) - H_O(\overrightarrow{m^t})]/(k_BT)\right) \\ &= \tau^{-1}W_0\left([H_O(\overrightarrow{m^h}) - H_O(\overrightarrow{m^t})]/(k_BT)\right) \\ &= \tau^{-1}W_0(\overrightarrow{m^t},\overrightarrow{m^h}), \end{aligned} \qquad \text{(S9)}$$

where τ is the microscopic time scale and W_0 is a dimensionless transition rate function that does not depend on τ. More details about the transition rate prescription chosen, the starting and ending states of the simulations and the architecture of the protein constructs simulated in this study can be found in Section S2.4.

Since the number of outgoing transitions from each state is as small as *N*, for the simulations it is convenient to use the kinetic Monte Carlo algorithm (9). According to this algorithm each transition requires the generation of two uniform random numbers in the interval (0, 1], one used to select the time to the next transition and the other one used to select one of the outgoing transitions from the current state (see Section S2.3).

S2. Materials and methods

S2.1 GTFEs and ASAs

In order to apply Eq. 6 at different DMSO concentrations we linearly interpolated the experimental transfer free energies of the full amino acids Glycine, Alanine, Leucine and Tryptophan, computed from the logarithm of solubility ratios reported in Table 7 of Ref. (10). The transfer free energies at DMSO concentrations of 50%, 40%, 30%, 20% and 10%, respectively, computed as (i) 2.81, 2.21, 1.34, 0.89 and 0.35 k_BT, respectively, for Glycine; (ii) 2.20, 1.75, 1.12, 0.73 and 0.30 k_BT, respectively, for Alanine; (iii) 1.90, 1.51, 0.97, 0.62 and 0.26 k_BT, respectively, for Leucine; and (iv) -0.52, -0.41, -0.38, -0.34 and -0.19 k_BT, respectively, for Tryptophan. Free energies of transfer for the side-chains of the above mentioned amino-acids $g^{ref}_{sc,R[k]}$ were estimated by subtracting the free energy of transfer of Glycine, which

is denoted by $g^{ref}_{bb,R[k]}$ in Eq. 6, and set to zero for all the other sidechains. As reference state we took the full amino acids, which is compatible with the type of solubility experimental data of Ref. (10). The amino acid structures were created and optimized using PRODRG2 (11). On the optimized structures we computed accessible surface areas for the backbone unit $A^{ref}_{bb,R[k]}$ and side chains $A^{ref}_{sc,R[k]}$ of the amino acids using PyMOL (12) with a probe radius of 0.14 nm.

For glycerol we applied the statistical mechanics model of Ref. (13) to estimate the transfer free energy of a backbone unit to the concentration of 30% v/v glycerol, obtaining the value of 0.42 k_BT (2). In this case the reference state was the backbone unit from the Gly-X-Gly tripeptide, with accessible surface areas taken from Table 2 in the Supplementary Information of Ref. (14). Side chains were not included in the glycerol calculations.

For GndCl we applied the same statistical mechanics model of Ref. (13) to estimate the transfer free energy of the backbone unit at GndCl concentrations of 3.04, 2.25 and 1 M, obtaining the values -0.26, -0.20 and -0.10 k_BT, respectively. As for glycerol, the reference state was taken to be the backbone unit from the Gly-X-Gly tripeptide, and side-chains were ignored.

For urea we used again the statistical mechanics model of Ref. (13) for the backbone unit of the Gly-X-Gly tripeptide, taken as the reference state. The transfer free energy of the backbone unit in 4 M urea computed as -0.26 k_BT and we ignored all sidechain contributions.

We computed the ASA of the native stretches split between backbone and sidechain atoms using PyMOL with a probe radius of 0.14 nm, while the ASA of the denatured state of GB1 and I27 was estimated using ProtSA (15, 16).

S2.2 Fitting the model

We extracted the native structure of GB1 and I27 (see Fig. 1) from the Protein Data Bank (PDB) (17), PDB codes 1PGA (18) and 1TIT (19), respectively. We removed the hetero-atoms from the structure after which we added the missing hydrogen atoms and flipped residue 8 of GB1 and residue 31 of I27 using MolProbity (20). Subsequently the MolProbity optimized structures were used for all calculations involving the structure of the native stretches of GB1 and I27.

We adopted the convention that all peptide bonds have the same entropic cost for being in the native state, i.e., $q_i = q$ for all $1 \le i \le N$, which is a commonly adopted assumption with WSME-like models (2, 4, 21). For any given value of q, the parameter ϵ can be obtained by imposing the value of the unfolding temperature onto the model.

As the unfolding temperature of GB1 we used the value 350.15 K obtained from a computational study at pH 7 (22). Note that this unfolding temperature is higher than the one used in a previous WSME study of GB1 (2), which in turn was the experimental unfolding temperature of a less thermally stable GB1 mutant (23). We performed a space search of q to find the value that gives a folded fraction of GB1 of 1/2 in the presence of 4 M urea at a temperature of 295.15 K (24). The simultaneous fit of q and ϵ led to the approximate values q=0.59 and ε=37.19.

From the previously characterized folding and unfolding kinetics of GB1 under mechanical tension at 301.15 K (25, 26), we estimated the unfolding force of GB1 to be $F_u = k_B T \ln[k_f(0)/k_u(0)]/(\Delta x_f + \Delta x_u) = 14.55$ pN where $k_f(0)$ is the spontaneous folding rate, $k_u(0)$ is the spontaneous unfolding rate, Δx_f is the folding distance and Δx_u is the unfolding distance. Imposing the above mentioned unfolding force and discretizing the native stretch contour lengths with a resolution of 0.01 nm we obtained the approximate value of ξ=0.34.

Similarly, we determined the parameters q, ϵ and ξ for I27 by using the unfolding temperature of 344.95 K (obtained by digitizing Fig.~(6) of Ref. (27) for pH 7.0), the denaturing concentration of 3.04 M GndCl at 298.15 K (28) and the unfolding force of 13.7 pN (29) at 298.15 K. We obtained the approximate values q=0.64, ε=41.76 and ξ=0.35.

S2.3 Kinetic Monte-Carlo algorithm

We show next the formulae used to implement the kinetic Monte Carlo algorithm in the force-clamp and velocity-clamp pulling modes. In what follows, let us denote the current state by $\overrightarrow{m^t}$, the N possible head states by $\overrightarrow{m^{h_1}}, \cdots, \overrightarrow{m^{h_N}}$ (the N head states can be taken in any order) and let u_1 and u_2 be two uniform random numbers in the interval (0,1].

S2.3.. Force-clamp simulations

For the force-clamp case, the time Δt before the next transition happens is given by the relation

$$\Delta t / \tau = -(\ln u_1) / \left[\sum_{i=1}^{N} W_0(\overrightarrow{m^t}, \overrightarrow{m^{h_i}}) \right], \tag{S10}$$

and the transition is performed to head state $\overrightarrow{m^{h_h}}$ with

$$h = \max_{1 \le i \le N} \left\{ i \,\middle|\, \sum_{j=1}^{i-1} W_0(\overrightarrow{m^t}, \overrightarrow{m^{h_j}}) / \sum_{j=1}^{N} W_0(\overrightarrow{m^t}, \overrightarrow{m^{h_j}}) < u_2 \right\}. \tag{S11}$$

It becomes clear from Eq. (S10) and Eq. (S11) that it is possible to perform force-clamp simulations without knowledge of the microscopic time scale τ, as long as it is understood that after the simulation the transition times obtained ($\Delta t/\tau$) need to be multiplied by τ for comparison with experimental data.

S2.3.2 Velocity-clamp simulations

Let us assume that the current time is t_s and that we need to compute the time to the next transition Δt, and then we need to find out which of the N possible transitions is taken. In what follows we use the notation

$$\begin{aligned} W_0(\overrightarrow{m^t}, \overrightarrow{m^h}, y) = W_0 \Big(\{ H_O(\overrightarrow{m^h}) - H_O(\overrightarrow{m^t}) + \\ \xi\kappa / 2 [x(\kappa, L(\overrightarrow{m^h}), v\tau y)^2 - x(\kappa, L(\overrightarrow{m^t}), v\tau y)^2] - \\ \xi\kappa v\tau y [x(\kappa, L(\overrightarrow{m^h}), v\tau y) - x(\kappa, L(\overrightarrow{m^t}), v\tau y)] \} / (k_B T) \Big) \end{aligned} \tag{S12}$$

where $x(\kappa,L,z)$ is the relevant root of Eq. 14 and $y \ge 0$ is a dimensionless quantity.

The time to the next transition Δt is given by the unique solution of the equation

$$\ln u_1 = -\sum_{i=1}^{N} \int_{t_s/\tau}^{t_s/\tau + \Delta t/\tau} W_0(\overrightarrow{m^t}, \overrightarrow{m^{h_i}}, y) dy \tag{S13}$$

and the transition is performed to head state $\overrightarrow{m^{h_h}}$ with

$$h = \max_{1 \le i \le N} \left\{ i \,\middle|\, \sum_{j=1}^{i-1} W_0(\overrightarrow{m^t}, \overrightarrow{m^{h_j}}, t_s/\tau + \Delta t/\tau) / \sum_{j=1}^{N} W_0(\overrightarrow{m^t}, \overrightarrow{m^{h_j}}, t_s/\tau + \Delta t/\tau) < u_2 \right\}. \tag{S14}$$

It becomes clear from Eq. (S13) and Eq. (S14) that while knowledge of τ is not strictly necessary to perform velocity-clamp simulations, knowledge of the product $v\tau$ is required. Moreover, after the simulation the transition times obtained ($\Delta t/\tau$) need to be multiplied by the microscopic time scale for comparison with experimental data.

Note that while Eq. (S13) is exact, solving it numerically requires repeated integration of an integrand that needs to solve numerically Eq. 14, and therefore becomes too slow in practice for low pulling velocities. The performance issue is circumvented by observing that at least for the exponential, Metropolis and Glauber transition rate expressions, $\int W_0(ay+b)dy$ has an analytical form (e.g., Eq. (S16)). Therefore we can solve Eq. (S13) by performing the integration on small steps of size $\Delta f/(\kappa v\tau)$, with Δf being the desired force resolution, in each step assuming that $x(\kappa,L,z)$ is constant and its value is given by solving numerically Eq. 14 at the beginning of the step, adding steps until $\ln u_1$ is exceeded. When that happens, the transition time is found numerically in the interval of the last added step, assuming again that $x(\kappa,L,z)$ is constant and equal to its exact value at the beginning of that last step.

S2.4 Mechanical unfolding simulations

Throughout all simulations we used the exponential transition rate prescription:

$$\begin{aligned} W_0(\overrightarrow{m^t},\overrightarrow{m^h}) &= W_0\left([H_O(\overrightarrow{m^h})-H_O(\overrightarrow{m^t})]/(k_BT)\right) \\ &= \exp\left(-[H_O(\overrightarrow{m^h})-H_O(\overrightarrow{m^t})]/(k_BT)/2\right). \end{aligned} \tag{S15}$$

The exponential transition rate, when composed with a linear function (see Section S2.3.2) integrates as

$$\int W_0(ay+b)dy = -2W_0(ay+b)/a. \tag{S16}$$

The force-dependent unfolding rate $k_u(f)$ was estimated as the inverse of the mean unfolding time over multiple trajectories, according to the formula $\langle t(F)\rangle = \int_0^\infty t k_u(F)\exp[-tk_u(F)]dt = 1/k_u(F)$. Then for each solvent condition separately, in order to estimate the two unfolding kinetic parameters, namely the spontaneous unfolding rate

$k_u(0)$ and unfolding distance Δx_u, we fitted Bell's equation (30, 31) on the full range for forces:

$$\ln k_u(F) = \ln k_u(0) + F\Delta x_u / (k_B T). \qquad \text{(S17)}$$

Some previous mechanical unfolding with WSME-like models considered the protein to be unfolded as soon as its extension reaches either half (3, 4, 21) or two thirds (3) of its maximum value. However WSME-like models tend to be less cooperative than the real proteins they describe (32), and their low cooperativity becomes most evident in velocity-clamp simulations where it results in multiple force-distance peaks for each module (not shown). Therefore we considered a protein domain to be unfolded as soon as all contacts between the force-bearing beta strands were lost (see Ref. (33) for a similar approach).

Using the procedure described in the main text, the following contacts were identified between the two force-bearing terminal beta strands of GB1 (34-36): (1, 49), (3, 44), (3, 49), (3, 51), (4, 49), (4, 50), (4, 51), (5, 51), (6, 50), (6, 51), (6, 52), (6, 53), (7, 53), (8, 53), (8, 54), (8, 55), (9, 55), (10, 55).

For the GB1 force-clamp mechanical unfolding simulations we used as a starting state one GB1 domain fully in the native state ($m_i = 1$ for all $1 \le i \le N$) and we regarded a trajectory as finished as soon as the protein unfolded.

For the GB1 velocity-clamp simulations we obtained the starting state by linking together 8 (eight) GB1 modules using 7 (seven) linker peptide bonds of length 0.4 nm, construct that we shall refer to as $(GB1)_8$. The linker peptide bonds were fixed in the non-native state all throughout the simulations. The starting state was constructed by putting in the native state all GB1 (non-linker) peptide bonds. As soon as a GB1 module unfolded, all its peptide bonds were fixed into the non-native state. A velocity-clamp trajectory was ended as soon as all the GB1 modules reached the unfolded state.

Since I27 unfolds mechanically through a metastable intermediate which has strand A detached (37), we fixed the state of the peptide bond 10 to denatured all throughout the simulations so as to avoid any contacts between strands A and G. Therefore our simulations of I27 describe the unfolding of the intermediate state, the same process that is most commonly observed in AFM experiments with I27 (38). Using the procedure described in the main text, the following contacts were identified between the force-bearing beta strands A' and G of I27's metastable intermediate: (11, 82), (11, 83), (11, 84), (12, 83), (12, 84),

(12, 86), (13, 83), (13, 84), (13, 85), (13, 86), (14, 86), (14, 87), (14, 88), (15, 85), (15, 86), (15, 87).

For both the force-clamp and velocity-clamp simulations of I27 we used as a starting state one I27 domain with all peptide bonds except the 10^{th} one in the native state ($m_i = 1 - \delta_{i,10}$ for all $1 \le i \le N$) and we regarded a trajectory as finished as soon as the protein unfolded, i.e., when all its critical contacts were lost.

The force-step size used for the performance optimization described in Section S2.3.2 for velocity-clamp simulations was $\Delta f = 1$ pN. For each unfolding event we recorded i) the contour length just before unfolding, which was taken as an approximation to be the contour length for all the stretching time range since the previous unfolded event, if any, or otherwise since the start of the trajectory, ii) the unfolding force, iii) the number of modules not-yet-unfolded in the construct (for the multimodular $(GB1)_8$), and iv) the force immediately after the previous unfolding event (for the multimodular $(GB1)_8$), or 0 pN for the first unfolding module in the trajectory. The recorded parameters were then used to perform Maximum-Likelihood (ML) estimation of the unfolding kinetic parameters (39).

For the persistence length of Eq. 8 we used the fixed value $p_l = 0.35$ nm (40) all throughout.

S2.5 Viscosity adjustment of the spontaneous unfolding kinetics inferred from the experimental data

Kramers theory predicts that

$$k_u(0) = A / \gamma exp[-\Delta G_u / (k_B T)] \qquad \text{(S18)}$$

where A is a constant, ΔG_u is the height of the unfolding activation barrier and γ is the reaction friction (41). The unfolding free energy difference in two different conditions, denoted below by superscripts $C1$ and $C2$, computes as

$$\Delta\Delta G_u = -k_B T \ln\{[\gamma^{C1} k_u^{C1}(0)] / [\gamma^{C2} k_u^{C2}(0)]\}, \qquad \text{(S19)}$$

assuming the constant A is the same in the two conditions.

According to Kramers theory, the friction coefficient γ is an abstraction standing for all the ways by which energy can be dissipated out of the reaction coordinate, direct dissipation into the solvent being

but one such mechanism. In particular, there need not be a simple relationship between γ and solvent viscosity (41).

The simple relationship

$$\gamma = 1/\eta \tag{S20}$$

where η is the solvent viscosity, was found in a few instances to result in good agreement with experimental data on protein folding and unfolding (42-47). Eq. (S20) has been sometimes used to account for viscosity effects in the interpretation of single-molecule mechanical folding and unfolding experiments (2, 25, 48).

However there is abundant experimental evidence that the dependency of Kramers' friction coefficient γ on solvent viscosity η is noticeably weaker than 1/η (49-55). Herein we adopt another, potentially more accurate formula for the friction coefficient that also takes into account the internal friction of the protein:

$$\gamma = 1/(\sigma + \eta), \tag{S21}$$

where $\sigma = 4\,cP$ is an estimate of the protein internal viscosity (55). Therefore when comparing to the unfolding activation barrier changes from the SMFS experiments of Ref. (2, 25), the experimentally inferred values reported in TABLE S 1 have been re-adjusted for viscosity using Eq. (S21) instead of Eq. (S20).

Moreover, the spontaneous rate of unfolding of I27 in the presence of glycerol 30% v/v reported in the last column of TABLE S 6 was also adjusted using Eq. (S21) (see Section S2.9).

S2.6 Polyprotein design and expression

We followed the protein construct design proposed by Prof. Julio Fernandez (Columbia University) for the study of the random coiled titin N2B segment (56). Chimeric polyproteins were obtained starting from pAFM1-4 and pAFM5-8 vectors, gently provided by Prof. Jane Clarke (Cambridge University) and constructed according to Ref. (57). The eight I27 module plasmid was reconstituted from pAFM1-4 and pAFM5-8, obtaining the pAFM8m vector. The plasmid was transformed into E. coli C41(DE3) cells (58) (obtained from Prof. John E. Walker (MRC - Dunn Human Nutrition Unit, Cambridge) with the agreement of the Medical Research Council centre of Cambridge). The cells were grown and the expression of proteins was induced as described in Ref. (57). Recombinant proteins were purified by Ni^{2+}-affinity chromatography in 20 mM sodium phosphate buffer pH 8, 500 mM NaCl; the elution from resin was obtained with 20 mM imidazole.

After purification the protein was kept at 193.15 K with glycerol 15% v/v.

S2.7 Single molecule force spectroscopy experiments

Constant velocity mechanical unfolding experiments were performed with a Veeco Picoforce Atomic Force Microscope (AFM) equipped with a DI Multimode Nanoscope IIIa controller (Bruker) and gold-coated, V-shaped silicon nitride cantilevers (NPG model; Bruker) with a nominal spring constant of 0.06 N/m. Unfolding experiments were performed on the homomeric polyprotein $(I27)_8$ in two different solvent conditions. In the first condition we used standard PBS buffer at pH 7.0. In the second condition we used the same buffer but in the presence of glycerol as a cosolvent, at a final concentration of 30% v/v. All the experiments have been performed at a temperature of approximately 301.15 K. For the experiments, a drop of the $(I27)_8$-containing solution ($5\mu L$, ~0.1 g/L) was deposited on a flame cleaned glass coverslip for about 20 minutes. The fluid cell was then filled with either the plain buffer or the glycerol-containing buffer, and sealed on top of the coverslip. Thermal tuning was performed in the respective solution to determine the cantilever spring constant. Pulling experiments were then started after a few minutes of incubation.

At the constant pulling velocities of 50.1, 100, 198, 513, 969, 2180 and 4360 nm/s we recorded i) 12, 24, 32, 27, 39, 148, and 160 unfolding events, respectively, from 1, 2, 3, 4, 4, 7 and 7 different experiments, respectively in plain buffer, and ii) 21, 24, 93, 124, 133, 151, and 362 unfolding events, respectively, from 2, 3, 5, 5, 5, 3, and 6 experiments, respectively with glycerol as cosolvent. Data filtering and extraction were performed using Hooke (59).

S2.8 Adjusting forces for viscosity

We computed the viscosity of the 30% v/v glycerol solution at 301.15 K as 2.357 cP using a formula reported elsewhere (60).

Immersion in a liquid environment dramatically alters the thermal noise spectrum of the cantilever, due to the strong effects of fluid loading (61-63). Problems in the determination of the spring constant arise when the resonance frequency drops to 1 kHz or below, as it happens for soft cantilevers or highly viscous media (61). However in the presence of 30% v/v glycerol as a cosolvent the resonance frequency of our cantilevers stays above 2 kHz, above the frequency

range likely to result in viscosity-induced errors in spring constant determination that are comparable to the error intrinsic to the thermal tuning method (64). Indeed, by calibrating a set of three cantilevers in both conditions we obtained an error of about 1.5% between the two conditions.

The measured unfolding forces are underestimated in high-viscosity solutions due to the viscous drag on the AFM cantilever (65-68). A way to remove this artifact has been recently reported (65). According to the this procedure the drag force can be computed as

$$F_{vis} = b_l v_{liquid} - b_c v_{tip}, \tag{S22}$$

where v_{liquid} is the pulling velocity, v_{tip} is the velocity of the tip, b_l and b_c are viscous drag coefficients related to the liquid motion and the bending of the cantilever (tip motion), respectively. These two parameters depend on tip-surface separation according to the formulae

$$b_l = 6\pi\eta a_l^2 / (s + h_l) \tag{S23}$$

and

$$b_c = 6\pi\eta a_c^2 / (s + h_c) \tag{S24}$$

where *s* is the tip-sample separation, η is the solvent viscosity, a_l, h_l, a_c and h_c being parameters to be determined. We extracted the mentioned parameters by fitting Eq. (S23), (S24) to the b_l and b_c values reported in Fig. 3 of Ref. (65), obtaining the approximate values $a_l = 24.3\mu m$, $h_l = 3.5\mu m$, $a_c = 19.8\mu m$ and $h_c = 2.9\mu m$. We then adjusted the force values collected at each sampled tip-surface separation in the experimental data taken in 30% v/v glycerol according to Eq. (S22). The average unfolding forces at 50.1, 100, 198, 513, 969, 2180 and 4360 nm/s increased by 0.01, 0.02, 0.10, 0.22, 0.44, 1.00 and 2.68 pN, respectively.

S2.9 Extracting the unfolding kinetics of I27 from SMFS velocity-clamp data

The unfolding kinetics of I27 at different pulling velocities were well described by Bell's model given in Eq. (S17). Maximizing the likelihood of the I27 SMFS data (39) we obtained $\Delta x_u = 0.25$ nm in the absence of glycerol and $\Delta x_u = 0.23$ nm in the presence of glycerol 30% v/v. Since the difference is likely within experimental error, we inferred that the presence of glycerol does not change the characteristic

unfolding distance of I27. Taking into account as well existing estimates of the unfolding distance of I27 (48, 69) we fixed the unfolding distance of I27 to $\Delta x_u = 0.25\,\text{nm}$ in both conditions, obtaining $k_u(0) = 0.001314 \pm 0.000067 s^{-1}$ in the absence of glycerol and $k_u(0) = 0.000256 \pm 0.000009 s^{-1}$ in the presence of glycerol 30% v/v.

If we consider as a first approximation that the prefactor *A* of Eq. (S18) is not affected by the addition of glycerol, taking the ratio of the logarithm of the estimated spontaneous unfolding rates in the two solvent conditions we obtained that the presence of glycerol at a concentration of 30% v/v increases the unfolding energy activation barrier of I27 by $\Delta\Delta G_u = 1.63 \pm 0.06 k_B T$. By further adjusting for the viscosity effects on the unfolding kinetics via Eq. (S21), we obtained our final estimate of $\Delta\Delta G_u = 1.36 \pm 0.06 k_B T$.

S3 Results and discussion

S3.1 Thermodynamics

We projected the free energy landscape of GB1 onto the non-mechanical reaction coordinate given by the weighted number of native contacts (see Section S1.1), which has been proposed as a good order parameter for protein folding and unfolding (3). We performed the projection in the absence of osmolytes and in the presence of i) DMSO 50%, 40%, 30%, 20% and 10% v/v, ii) glycerol 30% v/v, and finally iii) GndCl 2.25 and 1 M, conditions for which SMFS experimental data are available (2, 25, 70). The projection of the energy landscape in some of the mentioned solvents is shown in FIGURE S 1.

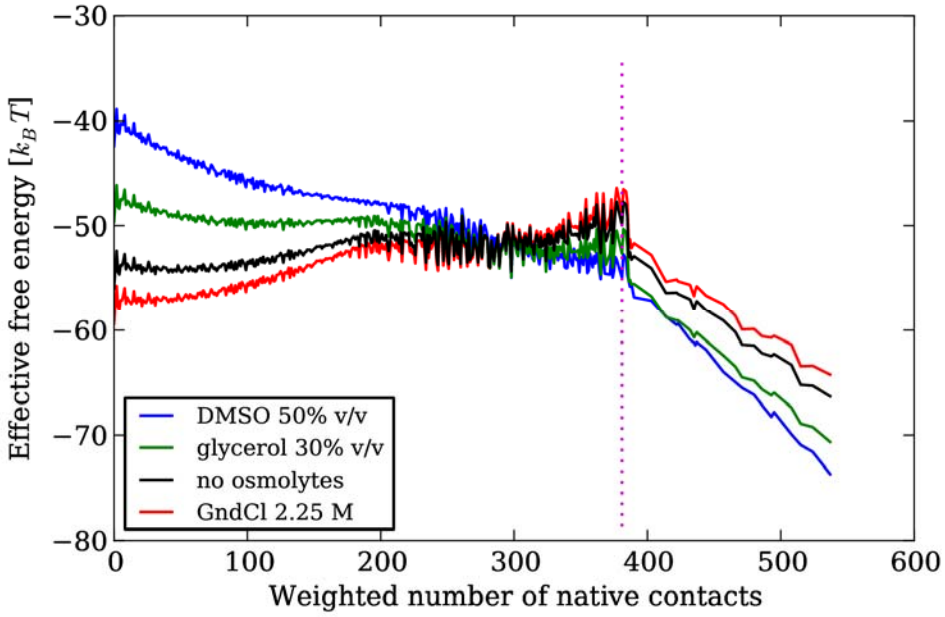

FIGURE S 1 Energy landscape of protein GB1 projected onto the reaction coordinate given by the weighted number of native contacts $\phi(\vec{m})$, as defined by Eq. (S3), in the absence of osmolytes, and in the presence of DMSO 50% v/v, glycerol 30% v/v and GndCl 2.25 M. The vertical bar at a weighted number of native contacts of 381 denotes the approximate position of the transition state.

If we make the simplifying assumption that the protein diffuses on the chosen reaction coordinate, we can in principle locate the transition state and measure its height. But the obtained energy landscape has a high degree of frustration, as seen in FIGURE S 1, which interferes with the significance and correct determination of the transition state (71). Therefore we computed a Boltzmann-weighted moving average of the energy landscape with a window size of five distinct neighboring populated reaction coordinate values (see FIGURE S 2), and we located the transition state by finding the maximum energetic level with the reaction coordinate value greater than or equal to 324. For DMSO 50% v/v and DMSO 40 % v/v the energy landscape as projected onto the weighted number of native contacts does not show any significant minimum for the unfolded state, making it impossible to identify a transition state. For all the other conditions, the described procedure identified the transition state at the same reaction coordinate value of 381 weighted native contacts and it measured changes in the unfolding activation energy barrier relative to the absence of osmolytes as indicated in TABLE S 1. Although the activation barrier changes from in-bulk experiments are not necessarily comparable to those from

SMFS experiments, the activation barrier changes estimated from the thermodynamic analysis based on the weighted number of native contacts agree qualitatively with the SMFS experimental ones.

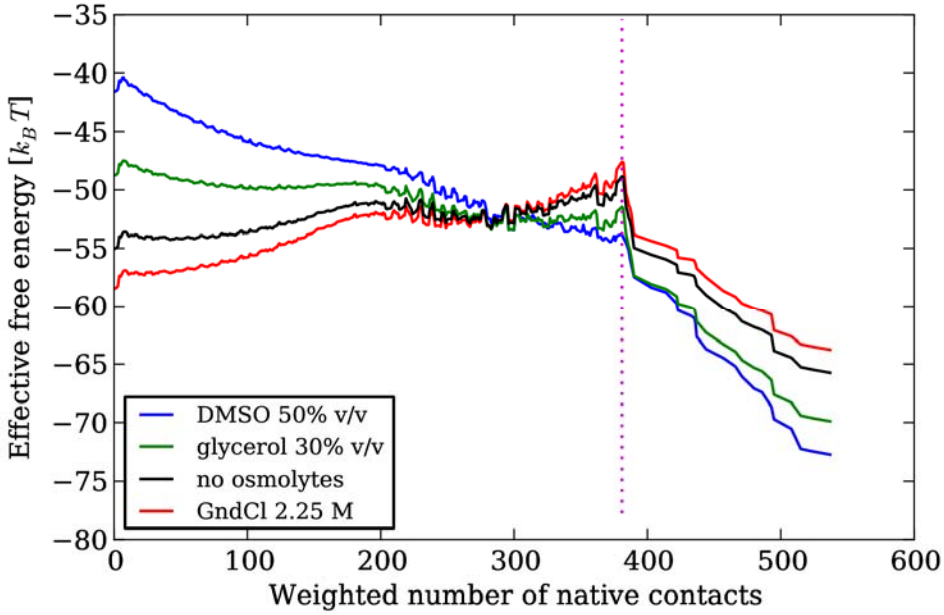

FIGURE S 2 Boltzmann-weighted moving average of the effective free energy of protein GB1 as a function of the weighted number of native contacts $\phi(\vec{m})$, as defined by Eq. (S3), in the absence of osmolytes, and in the presence of DMSO 50% v/v, glycerol 30% v/v and GndCl 2.25 M. The vertical bar at a weighted number of native contacts of 381 denotes the approximate position of the transition state.

TABLE S 1 GB1 activation barrier height changes. The column $\Delta\Delta G_u\,[k_B T]$ indicates the activation barrier height change calculated from the thermodynamic analysis based on the weighted number of native contacts. The last column contains the activation barrier changes estimated from SMFS velocity-clamp experiments (2, 25, 70) adjusted for viscosity as described in Section S2.5.

Solvent	$\Delta\Delta G_u\,[k_B T]$	SMFS $\Delta\Delta G_u\,[k_B T]$
DMSO 50%v/v	-	1.89
DMSO 40% v/v	-	1.00
DMSO 30% v/v	1.19	0.66
DMSO 20% v/v	0.74	0.30
DMSO 10% v/v	0.28	0.04
glycerol 30% v/v	1.71	1.60
no osmolytes	0	0
GndCl 2.25 M	-0.82	-2.38
GndCl 1 M	-0.41	-0.94

We also projected the free energy landscape of I27 onto the non-mechanical reaction coordinate given by the weighted number of native contacts, in the absence of osmolytes and in the presence of glycerol 30% v/v. As can be seen in FIGURE S 3, the energy landscape of I27 shows little unfolding cooperativity, which is expected considering that I27 has an unfolding intermediate that is stable over AFM timescales (37). Therefore this energy projection method does not make it possible to clearly identify an unfolding transition barrier for protein I27.

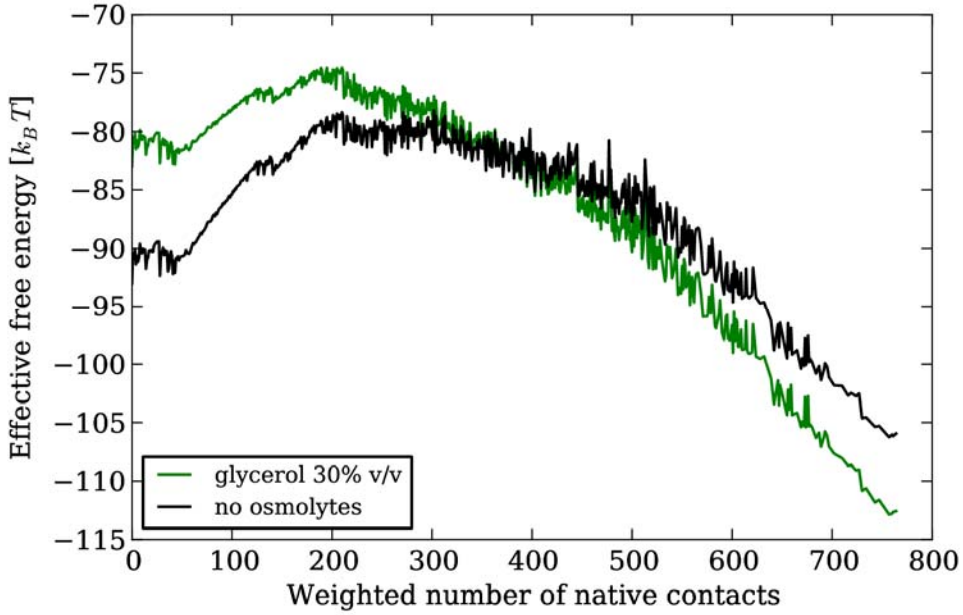

FIGURE S 3 Energy landscape of protein I27 projected onto the reaction coordinate given by the weighted number of native contacts $\phi(\vec{m})$, as defined by Eq. (S3), in the absence of osmolytes and in the presence of glycerol 30% v/v.

S3.2 Kinetics

S3.1.1 Force-clamp

TABLE S 2 Mechanical unfolding kinetic parameters from force-clamp simulations. The column $\Delta\Delta G_u$ [$k_B T$] is to be compared with column SMFS $\Delta\Delta G_u$ [$k_B T$] from **TABLE S 1**.

Solvent	Δx_u [nm]	$\Delta\Delta G_u$ [$k_B T$]
DMSO 50% v/v	0.134±0.003	1.717±0.279
DMSO 40% v/v	0.133±0.003	1.358±0.279

DMSO 30% v/v	0.131±0.003	0.862±0.279
DMSO 20% v/v	0.131±0.003	0.568±0.279
DMSO 10% v/v	0.129±0.003	0.203±0.279
glycerol 30% v/v	0.130±0.003	0.955±0.279
no osmolytes	0.128±0.003	0
GndCl 2.25 M	0.128±0.003	-0.450±0.279
GndCl 1 M	0.128±0.003	-0.192±0.279

TABLE S 3 Mechanical unfolding kinetic parameters of I27 from force-clamp simulations. The first three rows refer to the lower-force linear regime, while the last three rows refer to the higher-force linear regime. The estimation errors represent one standard deviation. For easy reference, the experimentally inferred $\Delta\Delta G_u$ in the presence of glycerol 30% v/v is $1.36 \pm 0.06 k_B T$, as computed in Section S2.9.

	no osmolytes	glycerol 30% v/v
I. Δx_u [nm]	0.197±0.045	0.203±0.041
I. $\Delta\Delta G_u$ [$k_B T$]	0	0.933±0.666
II. Δx_u [nm]	0.718±0.023	0.716±0.025
II. $\Delta\Delta G_u$ [$k_B T$]	0	1.336±1.179

S3.1.1 Velocity-clamp

TABLE S 4 Mean unfolding forces at three velocities from velocity-clamp experiments (2, 25, 70) and simulations with $(GB1)_8$.

Solvent	$F_{50.1}^{exp}$ [pN]	$F_{50.1}^{sim}$ [pN]	F_{400}^{exp} [pN]	F_{400}^{sim} [pN]	F_{4360}^{exp} [pN]	F_{4360}^{sim} [pN]
DMSO 50% v/v	200	350	-	-	300	539
DMSO 40% v/v	176	339	-	-	256	529
DMSO 30% v/v	172	318	-	-	244	515
DMSO 20% v/v	175	311	-	-	260	504
DMSO 10% v/v	139	293	-	-	240	495
glycerol 30% v/v	195	324	-	-	306	519
no osmolytes	119	278	178	-	253	485

GndCl 2.25 M	-	259	97	-	-	475
GndCl 1 M	-	268	148[4]	-	-	479

TABLE S 5 Mechanical unfolding kinetic parameters of GB1 from velocity-clamp simulations. The estimation errors represent one standard deviation and they have been computed via a bootstrap (case resampling) procedure, where for each velocity an equal number of traces were extracted with replacement, at least 100 times. The column $\Delta\Delta G_u$ [k_BT] is to be compared with column SMFS $\Delta\Delta G_u$ [k_BT] from **TABLE S 1**.

Solvent	Δx_u [nm]	$\Delta\Delta G_u$ [k_BT]
DMSO 50% v/v	0.086±0.0003	1.197±0.052
DMSO 40% v/v	0.086±0.0004	1.018±0.054
DMSO 30% v/v	0.085±0.0004	0.603±0.055
DMSO 20% v/v	0.085±0.0004	0.430±0.057
DMSO 10% v/v	0.085±0.0004	0.145±0.051
glycerol 30% v/v	0.085±0.0004	0.680±0.055
no osmolytes	0.085±0.0005	0
GndCl 2.25 M	0.084±0.0004	-0.355±0.056
GndCl 1 M	0.084±0.0004	-0.245±0.054

TABLE S 6 Mechanical unfolding kinetic parameters of I27 from velocity-clamp simulations. The estimation errors represent one standard deviation and they have been computed via a bootstrap (case resampling) procedure, where for each velocity an equal number of traces were extracted with replacement, at least 100 times. The column $\Delta\Delta G_u$ [k_BT] is to be compared with column $\Delta\Delta G_u^{exp}$ [k_BT], the latter indicating the experimentally inferred activation barrier changes.

Solvent	Δx_u [nm]	$\Delta\Delta G_u$ [k_BT]	$\Delta\Delta G_u^{exp}$ [k_BT]
glycerol 30% v/v	0.603±0.004	2.233±0.351	1.36±0.06
no osmolytes	0.590±0.004	0	0

[4] Obtained by digitizing Fig. 2 from Ref. 70.

Bibliography

1. Bruscolini, P., and A. Pelizzola. 2002. Exact solution of the Munoz-Eaton model for protein folding. Phys Rev Lett 88:258101.
2. Aioanei, D., I. Tessari, L. Bubacco, B. Samori, and M. Brucale. 2011. Observing the osmophobic effect in action at the single molecule level. Proteins.
3. Caraglio, M., A. Imparato, and A. Pelizzola. 2010. Pathways of mechanical unfolding of FnIII(10): low force intermediates. J Chem Phys 133:065101.
4. Imparato, A., A. Pelizzola, and M. Zamparo. 2007. Protein mechanical unfolding: a model with binary variables. J Chem Phys 127:145105.
5. Manousiouthakis, V. I., and M. W. Deem. 1999. Strict detailed balance is unnecessary in Monte Carlo simulation. Journal of Chemical Physics 110:2753-2756.
6. Crooks, G. E. 2000. Path-ensemble averages in systems driven far from equilibrium. Physical Review E 61:2361.
7. Muñoz, V., E. R. Henry, J. Hofrichter, and W. A. Eaton. 1998. A statistical mechanical model for beta-hairpin kinetics. Proc Natl Acad Sci U S A 95:5872-5879.
8. Mariz, A. M., F. D. Nobre, and C. Tsallis. 1994. Generalized single-spin-flip dynamics for the Ising model and thermodynamic properties. Phys Rev B Condens Matter 49:3576-3579.
9. Malvin H. Kalos, P. A. W. 2008. Monte Carlo Methods. Wiley-Vch Verlag Gmbh.
10. Arakawa, T., Y. Kita, and S. N. Timasheff. 2007. Protein precipitation and denaturation by dimethyl sulfoxide. Biophys Chem 131:62-70.
11. Schuttelkopf, A. W., and D. M. van Aalten. 2004. PRODRG: a tool for high-throughput crystallography of protein-ligand complexes. Acta Crystallogr D Biol Crystallogr 60:1355-1363.
12. Delano, W. L. 2002. The PyMOL Molecular Graphics System.
13. Street, T. O., D. W. Bolen, and G. D. Rose. 2006. A molecular mechanism for osmolyte-induced protein stability. Proc Natl Acad Sci U S A 103:13997-14002.
14. Auton, M., and D. W. Bolen. 2005. Predicting the energetics of osmolyte-induced protein folding/unfolding. Proc Natl Acad Sci U S A 102:15065-15068.
15. Bernado, P., M. Blackledge, and J. Sancho. 2006. Sequence-specific solvent accessibilities of protein residues in unfolded protein ensembles. Biophys J 91:4536-4543.

16. Estrada, J., P. Bernado, M. Blackledge, and J. Sancho. 2009. ProtSA: a web application for calculating sequence specific protein solvent accessibilities in the unfolded ensemble. BMC Bioinformatics 10:104.
17. Berman, H. M., J. Westbrook, Z. Feng, G. Gilliland, T. N. Bhat, H. Weissig, I. N. Shindyalov, and P. E. Bourne. 2000. The Protein Data Bank. Nucleic Acids Res 28:235-242.
18. Gallagher, T., P. Alexander, P. Bryan, and G. L. Gilliland. 1994. Two crystal structures of the B1 immunoglobulin-binding domain of streptococcal protein G and comparison with NMR. Biochemistry 33:4721-4729.
19. Improta, S., A. S. Politou, and A. Pastore. 1996. Immunoglobulin-like modules from titin I-band: extensible components of muscle elasticity. Structure 4:323-337.
20. Chen, V. B., W. B. Arendall, 3rd, J. J. Headd, D. A. Keedy, R. M. Immormino, G. J. Kapral, L. W. Murray, J. S. Richardson, and D. C. Richardson. 2010. MolProbity: all-atom structure validation for macromolecular crystallography. Acta Crystallogr D Biol Crystallogr 66:12-21.
21. Imparato, A., A. Pelizzola, and M. Zamparo. 2007. Ising-like model for protein mechanical unfolding. Phys Rev Lett 98:148102.
22. Wang, J., Z. Zhang, H. Liu, and Y. Shi. 2003. Quasiequilibrium unfolding thermodynamics of a small protein studied by molecular dynamics simulation with an explicit water model. Phys Rev E Stat Nonlin Soft Matter Phys 67:061903.
23. Lindman, S., W. F. Xue, O. Szczepankiewicz, M. C. Bauer, H. Nilsson, and S. Linse. 2006. Salting the charged surface: pH and salt dependence of protein G B1 stability. Biophys J 90:2911-2921.
24. Lv, S., D. M. Dudek, Y. Cao, M. M. Balamurali, J. Gosline, and H. Li. 2010. Designed biomaterials to mimic the mechanical properties of muscles. Nature 465:69-73.
25. Aioanei, D., S. Lv, I. Tessari, A. Rampioni, L. Bubacco, H. Li, B. Samori, and M. Brucale. 2011. Single-molecule-level evidence for the osmophobic effect. Angew Chem Int Ed Engl 50:4394-4397.
26. Aioanei, D., M. Brucale, and B. Samori. 2011. Open source platform for the execution and analysis of mechanical refolding experiments. Bioinformatics 27:423-425.
27. Politou, A. S., D. J. Thomas, and A. Pastore. 1995. The folding and stability of titin immunoglobulin-like modules, with implications for the mechanism of elasticity. Biophys J 69:2601-2610.
28. Fowler, S. B., and J. Clarke. 2001. Mapping the folding pathway of an immunoglobulin domain: structural detail from Phi value analysis and movement of the transition state. Structure 9:355-366.
29. Li H Fau - Linke, W. A., A. F. Linke Wa Fau - Oberhauser, M. Oberhauser Af Fau - Carrion-Vazquez, J. G. Carrion-Vazquez M Fau - Kerkvliet, H. Kerkvliet Jg Fau - Lu, P. E. Lu H Fau - Marszalek, J. M. Marszalek Pe Fau - Fernandez, and J. M. Fernandez. 2002. Reverse engineering of the giant muscle protein titin. Nature 418:5.
30. Bell, G. I. 1978. Models for the specific adhesion of cells to cells. Science 200:618-627.
31. Walcott, S. 2008. The load dependence of rate constants. J Chem Phys 128:215101.

32. Bruscolini, P., A. Pelizzola, and M. Zamparo. 2007. Downhill versus two-state protein folding in a statistical mechanical model. J Chem Phys 126:215103.
33. Caraglio, M., A. Imparato, and A. Pelizzola. 2011. Direction-dependent mechanical unfolding and green fluorescent protein as a force sensor. Phys Rev E Stat Nonlin Soft Matter Phys 84:021918.
34. Cao, Y., Y. D. Li, and H. Li. 2011. Enhancing the Mechanical Stability of Proteins through a Cocktail Approach. Biophys J 100:1794-1799.
35. Zheng, P., Y. Cao, T. Bu, S. K. Straus, and H. Li. 2011. Single molecule force spectroscopy reveals that electrostatic interactions affect the mechanical stability of proteins. Biophys J 100:1534-1541.
36. Cao, Y., and H. Li. 2007. Polyprotein of GB1 is an ideal artificial elastomeric protein. Nat Mater 6:109-114.
37. Taniguchi, Y., D. J. Brockwell, and M. Kawakami. 2008. The effect of temperature on mechanical resistance of the native and intermediate states of I27. Biophys J 95:5296-5305.
38. Best, R. B., S. B. Fowler, J. L. Herrera, A. Steward, E. Paci, and J. Clarke. 2003. Mechanical unfolding of a titin Ig domain: structure of transition state revealed by combining atomic force microscopy, protein engineering and molecular dynamics simulations. J Mol Biol 330:867-877.
39. Aioanei, D., B. Samori, and M. Brucale. 2009. Maximum likelihood estimation of protein kinetic parameters under weak assumptions from unfolding force spectroscopy experiments. Phys Rev E Stat Nonlin Soft Matter Phys 80:061916.
40. Carrion-Vazquez, M., P. E. Marszalek, A. F. Oberhauser, and J. M. Fernandez. 1999. Atomic force microscopy captures length phenotypes in single proteins. Proc Natl Acad Sci U S A 96:11288-11292.
41. Hagen, S. J. 2010. Solvent viscosity and friction in protein folding dynamics. Curr Protein Pept Sci 11:385-395.
42. Chrunyk, B. A., and C. R. Matthews. 1990. Role of diffusion in the folding of the alpha subunit of tryptophan synthase from Escherichia coli. Biochemistry 29:2149-2154.
43. Jacob, M., M. Geeves, G. Holtermann, and F. X. Schmid. 1999. Diffusional barrier crossing in a two-state protein folding reaction. Nat Struct Biol 6:923-926.
44. Plaxco, K. W., and D. Baker. 1998. Limited internal friction in the rate-limiting step of a two-state protein folding reaction. Proc Natl Acad Sci U S A 95:13591-13596.
45. Ramos, C. H., S. Weisbuch, and M. Jamin. 2007. Diffusive motions control the folding and unfolding kinetics of the apomyoglobin pH 4 molten globule intermediate. Biochemistry 46:4379-4389.
46. Perl, D., M. Jacob, M. Bano, M. Stupak, M. Antalik, and F. X. Schmid. 2002. Thermodynamics of a diffusional protein folding reaction. Biophys Chem 96:173-190.
47. Waldburger, C. D., T. Jonsson, and R. T. Sauer. 1996. Barriers to protein folding: formation of buried polar interactions is a slow step in acquisition of structure. Proc Natl Acad Sci U S A 93:2629-2634.
48. Dougan, L., A. S. Koti, G. Genchev, H. Lu, and J. M. Fernandez. 2008. A single-molecule perspective on the role of solvent hydrogen bonds in protein folding and chemical reactions. Chemphyschem 9:2836-2847.

49. Pabit, S. A., H. Roder, and S. J. Hagen. 2004. Internal friction controls the speed of protein folding from a compact configuration. Biochemistry 43:12532-12538.
50. Qiu, L., and S. J. Hagen. 2004. A limiting speed for protein folding at low solvent viscosity. J Am Chem Soc 126:3398-3399.
51. R. F. Grote, J. T. H. 1980. The stable states picture of chemical reactions. II. Rate constants for condensed and gas phase reaction models. J. Chem. Phys. 73:18.
52. Schlitter, J. 1988. Viscosity dependence of intramolecular activated processes. Chemical Physics 120:11.
53. Gouri S. Jas, W. A. E., James Hofrichter. 2001. Effect of Viscosity on the Kinetics of α-Helix and β-Hairpin Formation. The Journal of Physical Chemistry B 105:12.
54. Beece, D., L. Eisenstein, H. Frauenfelder, D. Good, M. C. Marden, L. Reinisch, A. H. Reynolds, L. B. Sorensen, and K. T. Yue. 1980. Solvent viscosity and protein dynamics. Biochemistry 19:5147-5157.
55. Ansari, A., C. M. Jones, E. R. Henry, J. Hofrichter, and W. A. Eaton. 1992. The role of solvent viscosity in the dynamics of protein conformational changes. Science 256:1796-1798.
56. Carrion-Vazquez, M., A. F. Oberhauser, T. E. Fisher, P. E. Marszalek, H. Li, and J. M. Fernandez. 2000. Mechanical design of proteins studied by single-molecule force spectroscopy and protein engineering. Progress in Biophysics and Molecular Biology 74:63-91.
57. Steward, A., J. L. Toca-Herrera, and J. Clarke. 2002. Versatile cloning system for construction of multimeric proteins for use in atomic force microscopy. Protein Sci 11:2179-2183.
58. Miroux, B., and J. E. Walker. 1996. Over-production of proteins in Escherichia coli: mutant hosts that allow synthesis of some membrane proteins and globular proteins at high levels. J Mol Biol 260:289-298.
59. Sandal, M., F. Benedetti, M. Brucale, A. Gomez-Casado, and B. Samori. 2009. Hooke: an open software platform for force spectroscopy. Bioinformatics 25:1428-1430.
60. Cheng, N.-S. 2008. Formula for the Viscosity of a Glycerol−Water Mixture. Industrial & Engineering Chemistry Research 47:3285-3288.
61. Pirzer, T., and T. Hugel. 2009. Atomic force microscopy spring constant determination in viscous liquids. Rev Sci Instrum 80:035110.
62. Sader, J. 1998. Frequency response of cantilever beams immersed in viscous fluids with applications to the atomic force microscope. Journal of Applied Physics 84:64-76.
63. Nicu, C. B. a. L. 2000. Viscosity measurements based on experimental investigations of composite cantilever beam eigenfrequencies in viscous media. Review of Scientific Instruments 71:5.
64. Christopher T. Gibson, D. J. J., Christopher Anderson, Chris Abell, and Trevor Rayment. 2004. Method to determine the spring constant of atomic force microscope cantilevers. Rev. Sci. Instrum. 75:3.
65. Liu, R., M. Roman, and G. Yang. 2010. Correction of the viscous drag induced errors in macromolecular manipulation experiments using atomic force microscope. Rev Sci Instrum 81:063703.

66. Vinogradova, O. I., H. J. Butt, G. E. Yakubov, and F. c. Feuillebois. 2001. Dynamic effects on force measurements. I. Viscous drag on the atomic force microscope cantilever. Review of Scientific Instruments 72:2330-2339.
67. Janovjak, H., J. Struckmeier, and D. J. Muller. 2005. Hydrodynamic effects in fast AFM single-molecule force measurements. Eur Biophys J 34:91-96.
68. Glasstone, S. 1941. The theory of rate processes: The kinetics of chemical reactions, viscosity, diffusion and electrochemical phenomena. McGraw-Hill Book Company, inc, New York.
69. Carrion-Vazquez, M., A. F. Oberhauser, S. B. Fowler, P. E. Marszalek, S. E. Broedel, J. Clarke, and J. M. Fernandez. 1999. Mechanical and chemical unfolding of a single protein: A comparison. Proceedings of the National Academy of Sciences of the United States of America 96:3694-3699.
70. Cao, Y., and H. Li. 2008. How do chemical denaturants affect the mechanical folding and unfolding of proteins? J Mol Biol 375:316-324.
71. Nymeyer, H., N. D. Socci, and J. N. Onuchic. 2000. Landscape approaches for determining the ensemble of folding transition states: success and failure hinge on the degree of frustration. Proc Natl Acad Sci U S A 97:634-639.